Exploratory X-Ray Monitoring of Luminous Radio-quiet Quasars at High Redshift: No Evidence for Evolution in X-Ray Variability

Ohad Shemmer[1] , W. N. Brandt[2,3,4] , Maurizio Paolillo[5,6,7] , Shai Kaspi[8], Cristian Vignali[9,10] ,
Paulina Lira[11], and Donald P. Schneider[2,3]

[1] Department of Physics, University of North Texas, Denton, TX 76203, USA; ohad@unt.edu
[2] Department of Astronomy and Astrophysics, 525 Davey Lab, The Pennsylvania State University, University Park, PA 16802, USA
[3] Institute for Gravitation and the Cosmos, The Pennsylvania State University, University Park, PA 16802, USA
[4] Department of Physics, 104 Davey Lab, The Pennsylvania State University, University Park, PA 16802, USA
[5] Dipartimento di Scienze Fisiche, Università Federico II di Napoli, via Cintia 6, I-80126 Napoli, Italy
[6] Agenzia Spaziale Italiana Science Data Center, Via del Politecnico snc, I-00133 Roma, Italy
[7] INFN - Unità di Napoli, via Cintia 9, I-80126, Napoli, Italy
[8] School of Physics & Astronomy and the Wise Observatory, Tel Aviv University, Tel Aviv 69978, Israel
[9] Dipartimento di Fisica e Astronomia, Alma Mater Studorium, Università degli Studi di Bologna, Via Gobetti 93/2, I-40129 Bologna, Italy
[10] INAF—Osservatorio Astronomico di Bologna, Via Gobetti 93/3, I-40129 Bologna, Italy
[11] Departamento de Astronomia, Universidad de Chile, Camino del Observatorio 1515, Santiago, Chile

Abstract

We report on the second installment of an X-ray monitoring project of seven luminous radio-quiet quasars (RQQs). New *Chandra* observations of four of these, at $4.10 \leqslant z \leqslant 4.35$, yield a total of six X-ray epochs per source, with temporal baselines of ∼850–1600 days in the rest frame. These data provide the best X-ray light curves for RQQs at $z > 4$ to date, enabling qualitative investigations of the X-ray variability behavior of such sources for the first time. On average, these sources follow the trend of decreasing variability amplitude with increasing luminosity, and there is no evidence for X-ray variability increasing toward higher redshifts, in contrast with earlier predictions of potential evolutionary scenarios. An ensemble variability structure function reveals that their variability level remains relatively flat across ≈20–1000 days in the rest frame and it is generally lower than that of three similarly luminous RQQs at $1.33 \leqslant z \leqslant 2.74$ over the same temporal range. We discuss possible explanations for the increased variability of the lower-redshift subsample and, in particular, whether higher accretion rates play a leading role. Near-simultaneous optical monitoring of the sources at $4.10 \leqslant z \leqslant 4.35$ indicates that none is variable on ≈1 day timescales, although flux variations of up to ∼25% are observed on ≈100 day timescales, typical of RQQs at similar redshifts. Significant optical-X-ray spectral slope variations observed in two of these sources are consistent with the levels observed in luminous RQQs and are dominated by X-ray variations.

Key words: galaxies: active – quasars: individual (Q 0000–263, BR 0351–1034, PSS 0926+3055, PSS 1326+0743) – X-rays: galaxies

1. Introduction

X-ray variability provides an effective means of probing the inner ≈10 gravitational radii of active galactic nuclei (AGNs; e.g., Nandra et al. 1997; Uttley et al. 2002; Markowitz et al. 2003; O'Neill et al. 2005; Ponti et al. 2012; La Franca et al. 2014; Lanzuisi et al. 2014). One of the main characteristics of this phenomenon is that more luminous AGNs, generally harboring larger supermassive black holes (SMBHs), exhibit milder and slower X-ray variations (e.g., Lawrence & Papadakis 1993). A strong variability−luminosity anti-correlation has indeed been observed in nearby, low-luminosity AGN samples, but there were doubts as to whether this relation holds for luminous quasars, found mostly at $z \gtrsim 1$ (e.g., Almaini et al. 2000; Manners et al. 2002; Paolillo et al. 2004).

In order to test this anti-correlation up to the highest accessible redshifts, Shemmer et al. (2014, hereafter Paper I) launched a long-term X-ray monitoring survey, using the *Chandra X-ray Observatory* (hereafter *Chandra*; Weisskopf et al. 2000), of four luminous, carefully selected radio-quiet quasars (RQQs) at $4.10 \leqslant z \leqslant 4.35$ (hereafter, the "*Chandra* sources"); these sources were selected as the only luminous, type 1 RQQs at $z > 4$ that had two distinct X-ray epochs and were bright enough for economical X-ray monitoring. This sample was complemented by X-ray observations, using the *Swift Gamma-Ray*

Burst Explorer (hereafter *Swift*; Gehrels et al. 2004), of three similarly luminous RQQs at $1.33 \leqslant z \leqslant 2.74$, PG 1247+267, PG 1634+706, and HS 1700+6416 (hereafter, the "*Swift* sources"). The *Swift* monitoring was necessary for separating the potential effects of redshift on variability from those attributed to luminosity, given the strong $L - z$ dependence inherent in most quasar surveys. All of the *Chandra* and *Swift* sources are representative of highly luminous type 1 (i.e., unobscured) RQQs in terms of their X-ray, UV, and optical properties (see Paper I for more details).

Paper I described the sample selection and the observational strategy. It also presented the initial results of the project that covered ∼2−4 yr and ∼5−13 yr in the rest frame of the *Chandra* and *Swift* sources, respectively. The basic finding indicated that most of the luminous RQQs in our sample exhibited X-ray variability at a level comparable to that observed in lower-luminosity sources at lower redshift, implying that these sources vary more than expected from a simple extrapolation of the variability−luminosity anti-correlation. However, it was not clear whether this result could be attributed to an evolution of the X-ray variability properties, or other physical properties, of RQQs. Paper I attributed the excess X-ray variability to higher accretion rates in these sources, as may have been expected from certain model power spectral densities (PSDs) of AGNs (e.g.,

Table 1
Log of New *Chandra* Observations of the *Chandra* Sources

Quasar	α (J2000.0)	δ (J2000.0)	z	Galactic N_H [a] (10^{20} cm^{-2})	Cycle	Obs. Date	Obs. ID	Exp. Time[b] (ks)
Q 0000−263	00 03 22.9	−26 03 16.8	4.10	1.67	14	2013 Sep 5	14216	9.84
					15	2014 Sep 16	14217	9.34
BR 0351−1034	03 53 46.9	−10 25 19.0	4.35	4.08	14	2013 Jul 18	14219	9.84
					15	2014 Nov 26	14220	9.93
PSS 0926+3055	09 26 36.3	+30 55 05.0	4.19	1.89	14	2013 May 12	14210	4.90
					15	2014 Jan 18	14211	4.90
PSS 1326+0743	13 26 11.9	+07 43 58.4	4.17	2.01	14	2013 Dec 5	14213	4.90
					15	2014 Mar 12	14214	4.90

Notes.
[a] Obtained from Dickey & Lockman (1990) using the N_H tool at http://heasarc.gsfc.nasa.gov/cgi-bin/Tools/w3nh/w3nh.pl.
[b] The *Chandra* exposure time has been corrected for detector dead time.

McHardy et al. 2006; Papadakis et al. 2008), supported by Eddington-ratio estimates from their X-ray and/or optical spectra. This interpretation implicitly assumed that all the RQQs in Paper I had been monitored sufficiently long for their X-ray variability to increase at an ever slowing rate and perhaps even saturate (i.e., that no significant long-term variations were missed). The manifestation of such saturation is a flattening of the PSD, or the variability structure function (SF), at long timescales (e.g., Fiore et al. 1998, Paper I). The X-ray variability amplitude therefore depends, in a complicated way, not only on the SMBH mass and accretion rate, but also on the monitoring duration, which is affected by source redshift in uniform monitoring surveys (e.g., Papadakis et al. 2008). Since the SF of RQQs at the redshifts of our *Chandra* sources has not been investigated prior to this work, it was necessary to test the assumption about a potential flattening by additional monitoring that would also contribute to reducing the uncertainties associated with the variability measurements.

The main goals of the current work are to extend the temporal baseline of our *Chandra* sources, construct an ensemble X-ray variability SF for this sample, and test whether the excess X-ray variability persists. This paper is organized as follows. In Section 2, we present new *Chandra* observations of our *Chandra* sources and describe the data reduction and analysis. In Section 3, we discuss the results of our extended time-series analyses, including near-simultaneous optical photometry of the *Chandra* sources, and in Section 4, we summarize our main findings. Luminosity distances were computed using the standard cosmological model ($\Omega_\Lambda = 0.7$, $\Omega_M = 0.3$, and $H_0 = 70$ km s^{-1} Mpc^{-1}; e.g., Spergel et al. 2007).

2. Observations and Data Reduction

Paper I presented four X-ray epochs for each of our *Chandra* sources, obtained until 2012. In this work, we present two additional epochs per source, obtained with *Chandra* Advanced CCD Imaging Spectrometer (ACIS; Garmire et al. 2003) snapshot observations in Cycles 14 and 15 (2013–2014) that were free of background flaring; the observation log appears in Table 1. The configuration used for these observations was identical to our two previous *Chandra* epochs from Cycles 12 and 13 (see Paper I). Data reduction was performed as in Paper I using standard *Chandra* Interactive Analysis of Observations (CIAO)[12] V4.1

routines. The X-ray counts in the observed-frame ultrasoft band (0.3–0.5 keV), soft band (0.5–2 keV), hard band (2–8 keV), and full band (0.5–8 keV) were extracted with the WAVDETECT thread (Freeman et al. 2002) using wavelet transforms (with wavelet scale sizes of 1, 1.4, 2, 2.8, and 4 pixels) and a false-positive probability threshold of 10^{-3}; visual image inspection confirms the WAVDETECT photometric results. These X-ray counts, as well as those of the *Chandra* Cycles 12–13 observations from Paper I, are reported in Table 2.

For each source, Table 2 also lists the band ratio (defined as the hard-band counts divided by those in the soft band), the effective power-law photon index,[13] the soft-band count rate, and the Galactic absorption-corrected flux density at rest-frame 2 keV. Galactic absorption-corrected fluxes in the soft band were obtained using the *Chandra* PIMMS v4.7b tool, assuming a power-law model with $\Gamma = 2.0$. Five of the Cycle 12–13 observations were reprocessed during the *Chandra* X-ray Center (CXC) Fourth Reprocessing Campaign and are marked accordingly in Table 2. The counts from the reprocessed data are consistent with the respective counts in Table 4 of Paper I, within the errors. Inspection of Table 2 shows that the effective power-law photon index of each source has not changed significantly during *Chandra* Cycles 12 through 15; these photon indices are also consistent with those measured from X-ray imaging spectroscopy of the sources (Shemmer et al. 2005, and references therein).

3. Results and Discussion

3.1. New Variability Amplitudes

The total six-epoch X-ray fluxes of the *Chandra* sources are presented in Table 3, and the respective light curves are displayed in Figure 1. To the best of our knowledge, these light curves contain the largest number of distinct X-ray epochs, i.e., with sufficient number of counts, for any RQQ at $z > 4$, also spanning the longest temporal baseline (see, e.g., Paper I; Yang et al. 2016). Table 3 and Figure 1 include newly measured fluxes from archival *ROSAT* observations of Q 0000−263 and BR 0351−1034, where we have followed the steps outlined in Section 2.4 of Paper I. These new flux measurements,

---

[12] http://cxc.cfa.harvard.edu/ciao/

[13] The effective power-law photon index Γ, defined as $N(E) \propto E^{-\Gamma}$, was derived from the band ratio using the *Chandra* PIMMS v4.7b tool at http://cxc.harvard.edu/toolkit/pimms.jsp for each particular Cycle, assuming Galactic, and no intrinsic, absorption.

Table 2
Basic X-Ray Measurements from *Chandra* Observations of the *Chandra* Sources

| Quasar | Cycle | Counts[a] | | | | Band Ratio[b] | Γ[b] | Count Rate[c] | $f_{2\,\mathrm{keV}}$[d] |
		0.3–0.5 keV	0.5–2 keV	2–8 keV	0.5–8 keV				
Q 0000−263	12[e]	$4.0^{+3.2}_{-1.9}$	$54.3^{+8.4}_{-7.3}$	$14.8^{+4.9}_{-3.8}$	$69.0^{+9.4}_{-8.3}$	$0.27^{+0.10}_{-0.08}$	1.9 ± 0.3	$5.47^{+0.85}_{-0.74}$	1.7
	13	$4.9^{+3.4}_{-2.1}$	$44.7^{+7.7}_{-6.7}$	$18.6^{+5.4}_{-4.3}$	$63.3^{+9.0}_{-7.9}$	$0.42^{+0.14}_{-0.11}$	1.5 ± 0.3	$4.50^{+0.78}_{-0.67}$	1.4
	14	$2.0^{+2.6}_{-1.3}$	$30.6^{+6.6}_{-5.5}$	$11.7^{+4.5}_{-3.4}$	$42.4^{+7.6}_{-6.5}$	$0.38^{+0.17}_{-0.13}$	$1.6^{+0.4}_{-0.3}$	$3.10^{+0.67}_{-0.56}$	1.0
	15	$2.0^{+2.7}_{-1.3}$	$41.7^{+7.5}_{-6.4}$	$10.7^{+4.4}_{-3.3}$	$53.5^{+8.4}_{-7.3}$	$0.26^{+0.11}_{-0.09}$	2.1 ± 0.4	$4.47^{+0.80}_{-0.69}$	1.6
BR 0351−1034	12[e]	<3.0	$11.8^{+4.5}_{-3.4}$	$2.9^{+2.9}_{-1.6}$	$14.7^{+4.9}_{-3.8}$	$0.24^{+0.26}_{-0.15}$	$2.1^{+0.9}_{-0.7}$	$1.19^{+0.46}_{-0.34}$	0.4
	13[e]	<3.0	$9.8^{+4.3}_{-3.1}$	$2.9^{+2.9}_{-1.6}$	$12.7^{+4.7}_{-3.5}$	$0.29^{+0.32}_{-0.18}$	$1.9^{+0.9}_{-0.7}$	$1.00^{+0.43}_{-0.31}$	0.4
	14	<3.0	$19.8^{+5.5}_{-4.4}$	$5.9^{+3.6}_{-2.3}$	$25.6^{+6.1}_{-5.0}$	$0.30^{+0.20}_{-0.18}$	$1.9^{+0.6}_{-0.5}$	$2.01^{+0.56}_{-0.44}$	0.7
	15	<3.0	$15.0^{+5.0}_{-3.8}$	$8.8^{+4.1}_{-2.9}$	$23.8^{+6.0}_{-4.8}$	$0.59^{+0.34}_{-0.24}$	$1.3^{+0.5}_{-0.4}$	$1.51^{+0.50}_{-0.38}$	0.6
PSS 0926+3055	12[e]	$2.0^{+2.7}_{-1.3}$	$33.7^{+6.9}_{-5.8}$	$10.9^{+4.4}_{-3.3}$	$44.6^{+7.7}_{-6.6}$	$0.32^{+0.15}_{-0.11}$	$1.8^{+0.4}_{-0.3}$	$6.76^{+1.38}_{-1.16}$	2.2
	13	<4.8	$22.7^{+5.8}_{-4.7}$	$8.0^{+4.0}_{-2.8}$	$30.7^{+6.6}_{-5.5}$	$0.35^{+0.20}_{-0.14}$	$1.7^{+0.5}_{-0.4}$	$4.57^{+1.18}_{-0.95}$	1.5
	14	$3.9^{+3.2}_{-1.9}$	$41.4^{+7.5}_{-6.4}$	$14.8^{+4.9}_{-3.8}$	$56.1^{+8.5}_{-7.5}$	$0.36^{+0.14}_{-0.11}$	1.7 ± 0.3	$8.44^{+1.53}_{-1.31}$	2.7
	15	<6.4	$35.6^{+7.0}_{-5.9}$	$9.9^{+4.3}_{-3.1}$	$45.5^{+7.8}_{-6.7}$	$0.28^{+0.13}_{-0.10}$	2.0 ± 0.4	$7.25^{+1.43}_{-1.21}$	2.7
PSS 1326+0743	12[e]	$2.0^{+2.6}_{-1.3}$	$33.8^{+6.9}_{-5.8}$	$9.8^{+4.2}_{-3.1}$	$43.6^{+7.7}_{-6.6}$	$0.29^{+0.14}_{-0.10}$	1.9 ± 0.4	$6.78^{+1.38}_{-1.16}$	2.2
	13	$2.0^{+2.7}_{-1.3}$	$32.4^{+6.8}_{-5.7}$	$11.9^{+4.6}_{-3.4}$	$44.4^{+7.7}_{-6.6}$	$0.37^{+0.16}_{-0.12}$	$1.7^{+0.4}_{-0.3}$	$6.49^{+1.35}_{-1.13}$	2.1
	14	$3.0^{+2.9}_{-1.6}$	$26.6^{+6.2}_{-5.1}$	$4.0^{+3.2}_{-1.9}$	$30.6^{+6.6}_{-5.5}$	$0.15^{+0.12}_{-0.08}$	2.5 ± 0.6	$5.42^{+1.27}_{-1.04}$	1.8
	15	$3.0^{+2.9}_{-1.6}$	$37.4^{+7.2}_{-6.1}$	$11.9^{+4.6}_{-3.4}$	$51.2^{+8.2}_{-7.1}$	$0.37^{+0.15}_{-0.11}$	$1.7^{+0.4}_{-0.3}$	$7.67^{+1.47}_{-1.25}$	2.8

Notes.

[a] Errors on the X-ray counts, corresponding to the 1σ level, were computed according to Tables 1 and 2 of Gehrels (1986) using Poisson statistics. Upper limits are at the 95% confidence level, computed according to Kraft et al. (1991); upper limits of 3.0, 4.8, and 6.4 indicate that 0, 1, and 2 X-ray counts, respectively, have been found within an extraction region of radius $1''$ centered on the source's optical position (considering the background within this source-extraction region to be negligible).

[b] Errors at the 1σ level on the band ratio and effective photon index were computed following Section 1.7.3 of Lyons (1991); this method avoids the failure of the standard approximate-variance formula when the number of counts is small (see Section 2.4.5 of Eadie et al. 1971). The photon indices have been obtained using *Chandra* PIMMS v4.7b, which also implements the correction required to account for the Cycle-to-Cycle decay in quantum efficiency of ACIS at low energies (Townsley et al. 2000).

[c] Count rate computed in the soft band (observed-frame 0.5–2 keV) in units of 10^{-3} counts s^{-1}.

[d] Galactic absorption-corrected flux density at rest-frame 2 keV in units of 10^{-31} erg cm^{-2} s^{-1} Hz^{-1} assuming a power-law model with $\Gamma = 2.0$.

[e] Reprocessed during the CXC Fourth Reprocessing Campaign.

---

corresponding to the first X-ray epoch for each source, are lower than the fluxes reported in Paper I by factors of 1.4 and 3.9, respectively. The original fluxes from Paper I, given in the observed-frame 0.5–2 keV band, were derived from the corresponding fluxes in the observed-frame 0.1–2 keV band reported in Table 2 of Kaspi et al. (2000), using WebPIMMS,[14] assuming $\Gamma = 2.0$. The new fluxes reported in Table 3 were derived directly from the original *ROSAT* observations by filtering their event files in the observed-frame 0.5–2 keV band. Using the same *ROSAT* observations and employing a reduction technique similar to the one we use here, Vignali et al. (2001) obtained fluxes that are ∼10–15% higher than, but consistent within the errors with, the improved fluxes we obtain in this work. The differences between the newly derived fluxes and the original values reported in Paper I have no significant impact on the main results we present below.

Following the steps in Paper I, we first determined whether a source is variable by applying a χ^2 test to its entire light curve in the soft band; this band, in which we obtain the largest fraction of the total counts form each source, enables more meaningful comparisons with the X-ray variability of lower-redshift sources across similar rest-frame energy bands. The null hypothesis is that the flux in each epoch is consistent with the mean flux of the entire light curve, within the errors. This is

expressed as

$$\chi^2 = \frac{1}{N_{\mathrm{obs}} - 1} \sum_{i=1}^{N_{\mathrm{obs}}} \frac{(f_i - \langle f \rangle)^2}{\sigma_i^2}, \qquad (1)$$

where f_i and σ_i are the flux and its error for the ith observation, respectively, N_{obs} is the number of observations, and $\langle f \rangle$ is the unweighted mean flux of the light curve. We repeated the χ^2 test, restricting it to include only the *Chandra* observations of each source, in order to minimize the effects of observatory-dependent flux calibrations. For both tests, Table 4 gives the χ^2 values as well as the corresponding degrees of freedom (dof; where dof $= N_{\mathrm{obs}} - 1$) and the χ^2 distribution probability by which the null hypothesis can be rejected $(1 - p)$. Considering $p \geqslant 0.90$ as the criterion for variability, only Q 0000−263 remains variable, while BR 0351−1034 and PSS 0926+3055 are now considered non-variable, with respect to Paper I; PSS 1326+0743 remains non-variable.

When only their *Chandra* epochs are considered, none of the sources is variable (Table 4). Additionally, no significant X-ray spectral variations are detected in any of the *Chandra* sources, as can be inferred from their band ratios or effective photon indices in Table 2, consistent with the results of Paper I.

The X-ray variability amplitude (in terms of the excess variance, σ_{rms}^2) and its error for each *Chandra* source is given in Table 4 separately for the entire light curve and for the

---

[14] http://heasarc.gsfc.nasa.gov/cgi-bin/Tools/w3pimms/w3pimms.pl

Table 3
X-Ray Light Curve Data for the *Chandra* Sources

Quasar	JD	f_x [a]	Observatory	Reference
Q 0000−263	2448588.5	22 ± 3	*ROSAT*	1
	2452450.5	12.6 ± 0.7	*XMM-Newton*	2, 3, 4
	2455802.5	23^{+4}_{-3}	*Chandra*	5
	2456173.5	20 ± 3	*Chandra*	5
	2456540.5	13^{+3}_{-2}	*Chandra*	1
	2456917.0	20^{+4}_{-3}	*Chandra*	1
BR 0351-1034	2448647.5	15 ± 6	*ROSAT*	1
	2453035.5	12 ± 2	*XMM-Newton*	2, 4, 6
	2455827.5	5 ± 2	*Chandra*	5
	2455862.5	4^{+2}_{-1}	*Chandra*	5
	2456491.5	9^{+3}_{-2}	*Chandra*	1
	2456987.5	8^{+3}_{-2}	*Chandra*	1
PSS 0926+3055	2452344.5	30^{+5}_{-4}	*Chandra*	2, 7
	2453322.5	40 ± 3	*XMM-Newton*	2
	2455623.5	30^{+6}_{-5}	*Chandra*	5
	2455939.5	20^{+5}_{-4}	*Chandra*	5
	2456424.5	40 ± 6	*Chandra*	1
	2456675.5	30^{+7}_{-6}	*Chandra*	1
PSS 1326+0743	2452284.5	24 ± 4	*Chandra*	2, 7
	2453001.5	28^{+2}_{-3}	*XMM-Newton*	2
	2455627.5	30^{+6}_{-5}	*Chandra*	5
	2456047.5	30^{+6}_{-5}	*Chandra*	5
	2456632.5	20^{+5}_{-4}	*Chandra*	1
	2456729.0	40^{+7}_{-6}	*Chandra*	1

Note.

[a] Galactic absorption-corrected flux in the soft band (i.e., observed-frame 0.5–2 keV band) in units of 10^{-15} erg cm^{-2} s^{-1}.

References. (1) This work; (2) Shemmer et al. (2005); (3) Ferrero & Brinkmann (2003); (4) Grupe et al. (2006); (5) Paper I; (6) Grupe et al. (2004); (7) Vignali et al. (2003).

Chandra epochs only. The definitions of $\sigma^2_{\rm rms}$ and its error follow from Turner et al. (1999; see also Nandra et al. 1997), where

$$\sigma^2_{\rm rms} = \frac{1}{N_{\rm obs} \langle f \rangle^2} \sum_{i=1}^{N_{\rm obs}} [(f_i - \langle f \rangle)^2 - \sigma_i^2]; \qquad (2)$$

this parameter can be negative if the measurement errors are larger than the flux variance. The formal error on $\sigma^2_{\rm rms}$ is $s_D/(\langle f \rangle^2 \sqrt{N_{\rm obs}})$, where s_D follows from

$$s_D^2 = \frac{1}{N_{\rm obs} - 1} \sum_{i=1}^{N_{\rm obs}} \{[(f_i - \langle f \rangle)^2 - \sigma_i^2] - \sigma^2_{\rm rms} \langle f \rangle^2\}^2. \quad (3)$$

This expression only involves the measurement errors and does not take into account the scatter intrinsic to any red-noise random process, particularly in cases where the PSD shape is not known (see, e.g., Vaughan et al. 2003; Allevato et al. 2013). Estimating the red-noise contribution to the errors, in our case, requires detailed simulations that are not practical, given that our sources currently have only six X-ray epochs and there are essentially no constraints on their PSD slopes.

The variability amplitudes of the *Chandra* sources are consistent, within the errors, with those computed from the first four X-ray epochs (see Paper I, taking into account the new fluxes from the first epoch of both Q 0000−263 and BR 0351−1034). Considering only their *Chandra* epochs, the variability amplitudes
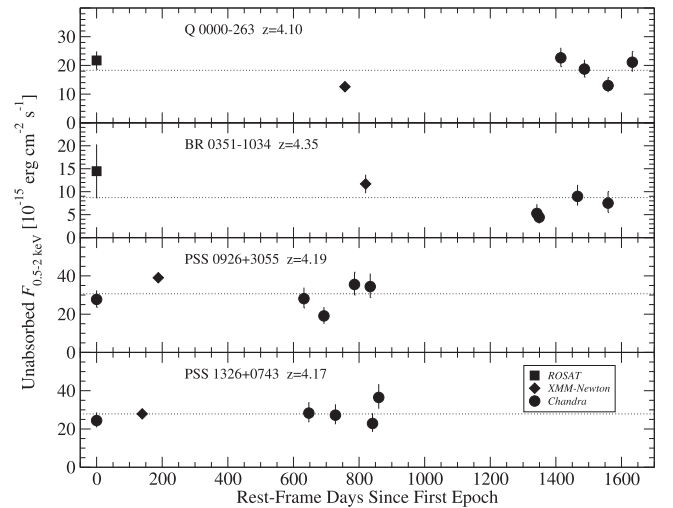

Figure 1. X-ray light curves of the *Chandra* sources. Galactic absorption-corrected flux in the soft band (i.e., the observed-frame 0.5–2 keV band) is plotted as a function of rest-frame time (in days) relative to the first X-ray epoch for each source. Squares, diamonds, and circles mark *ROSAT*, *XMM-Newton*, and *Chandra* observations, respectively. The dotted line in each panel indicates the mean flux.

of all the *Chandra* sources are consistent with zero and generally lower than those computed from their entire light curves. This result may stem from relying on a single observatory, thus eliminating inter-calibration effects that can mimic increased variability, and/or the fact that the last four *Chandra* epochs span only ∼220 days in the rest frame of each source, perhaps not sufficiently long to show pronounced variations (see below).

3.2. What Determines the X-Ray Variability Amplitude?

The quantity $\sigma^2_{\rm rms}$ essentially measures the light curve variance with respect to the measurement errors. The variance, σ^2, is derived from integrating the AGN PSD between a minimum and maximum frequency ($\nu_{\rm min}$ and $\nu_{\rm max}$, respectively),

$$\sigma^2 = \int_{\nu_{\rm min}}^{\nu_{\rm max}} \mathrm{PSD}(\nu)\, d\nu, \qquad (4)$$

and the PSD as a function of frequency, ν, is typically modeled by a broken (or bending) power law of the form,

$$\mathrm{PSD}(\nu) = A\nu^{-1}\left(1 + \frac{\nu}{\nu_{\rm b}}\right)^{-1}, \qquad (5)$$

where A is the PSD normalization and $\nu_{\rm b}$ is the break frequency (see, e.g., González-Martín & Vaughan 2012). Based on this simple functional form and the extended temporal baseline for the *Chandra* sources, one would have expected a general trend of increasing variability amplitudes with the addition of two epochs per source (e.g., Vagnetti et al. 2011). However, the increase of $\sigma^2_{\rm rms}$ can be insignificant since this parameter depends on the actual PSD power-law slope and the extension of the temporal baseline can introduce systematic effects and biases into its measured value. In particular, larger temporal gaps may form that can affect $\sigma^2_{\rm rms}$ by up to ∼30% (Allevato et al. 2013). We investigate the effects of the extended temporal
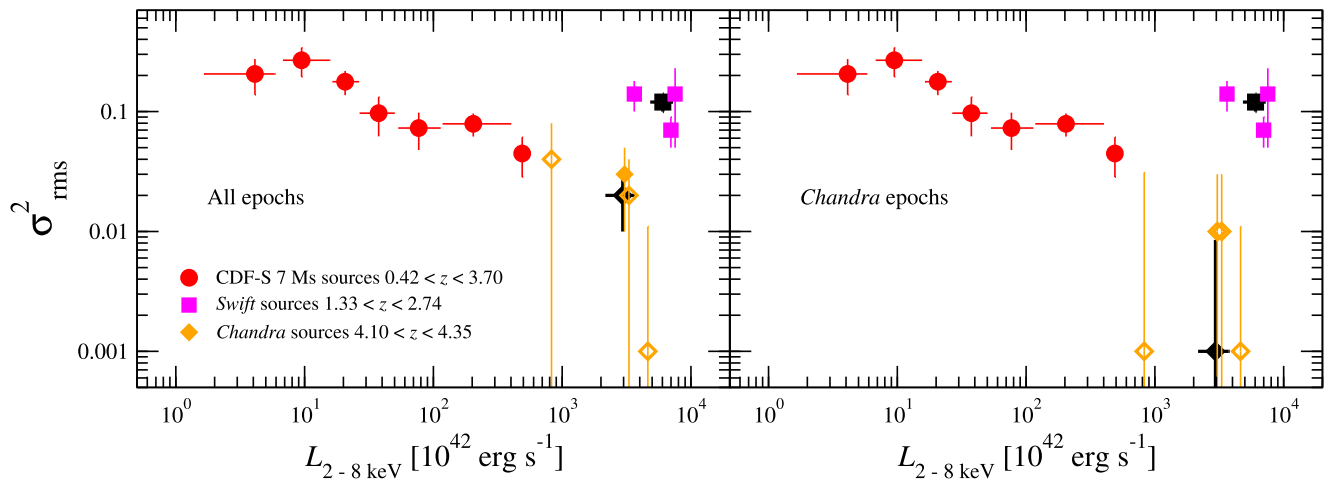
Figure 2. Excess variance vs. luminosity in the rest-frame 2–8 keV band. Circles represent average luminosities and σ^2_{rms} values of X-ray-selected AGNs, grouped in seven luminosity bins, from the 7 Ms exposure of the CDF-S survey (adapted from P17). Squares and diamonds represent the *Swift* and *Chandra* sources, respectively; open diamonds mark non-variable *Chandra* sources. Sources with negative σ^2_{rms} values have been pegged at $\sigma^2_{rms} = 0.001$. Error bars on σ^2_{rms} represent "formal" errors due only to flux measurement errors and not those due to red-noise intrinsic scatter. The black diamond and square represent the average σ^2_{rms} and $L_{2-8\,keV}$ values of our *Chandra* and *Swift* sources, respectively. The left (right) panel represents all (only the *Chandra*) epochs.

Table 4
X-Ray Variability Indicators in the Soft Band

Quasar	All Epochs			Chandra Epochs		
	χ^2(dof)	$1 - p$[a]	σ^2_{rms}	χ^2(dof)	$1 - p$[a]	σ^2_{rms}
Q 0000−263	13.9(5)	1.6×10^{-2}	0.03 ± 0.02	2.3(3)	5.0×10^{-1}	0.01 ± 0.02
BR 0351−1034	2.8(5)	7.3×10^{-1}	0.04 ± 0.04	1.2(3)	7.6×10^{-1}	-0.02 ± 0.03
PSS 0926+3055	3.8(5)	5.7×10^{-1}	0.02 ± 0.02	1.7(4)	7.8×10^{-1}	0.01 ± 0.02
PSS 1326+0743	0.7(5)	9.8×10^{-1}	-0.01 ± 0.01	0.9(4)	9.2×10^{-1}	-0.01 ± 0.01

Note.
[a] The probability p of the χ^2 distribution, given the χ^2 value and the degrees of freedom (dof).

baseline on the variability amplitudes of our *Chandra* sources below.

The variability amplitudes of our sources can be compared with those of X-ray-selected AGNs from the 7 Ms exposure of the *Chandra* Deep Field-South (CDF-S) survey, spanning more than 17 years in the observed frame (Luo et al. 2017). The σ^2_{rms} values for the CDF-S sources were measured by Paolillo et al. (2017; hereafter, P17) in the rest-frame 2–8 keV band of each source, primarily for minimizing the effects of variable obscuration. The P17 sample includes variable (with $p \geqslant 0.95$) and non-variable sources that have light curve signal-to-noise ratios (S/N) > 0.8 per bin (i.e., the average S/N across all epochs), and >90 points in each light curve. Sources considered to be radio loud, according to the criteria defined in Section 3.2 of Bonzini et al. (2013), were removed from the CDF-S sample in order to minimize potential jet-related variability. However, these criteria differ from those of Kellermann et al. (1989), which are commonly used for defining radio loudness in AGNs. Therefore, sources that are formally radio loud or radio intermediate may still remain in the sample.

The final CDF-S sample included 94 sources at $0.42 \leqslant z \leqslant 3.70$ (i.e., the "bright-R" sample of P17). Their intrinsic absorption column densities were estimated (from their soft- to hard-band ratios assuming a power-law slope of $\Gamma = 1.8$) by Luo et al. (2017) to lie in the range

$7.8 \times 10^{20}\ \mathrm{cm}^{-2} \lesssim N_H \lesssim 7.7 \times 10^{23}\ \mathrm{cm}^{-2}$ with a median value of $N_H \sim 3.7 \times 10^{22}\ \mathrm{cm}^{-2}$. Since the intrinsic absorption column densities of our *Chandra* sources are constrained to lie in the range $N_H \leqslant 0.40 - 5.29 \times 10^{22}\ \mathrm{cm}^{-2}$ (Shemmer et al. 2005), about half or more of these CDF-S sources have somewhat higher absorption in comparison. However, given the relatively mild obscuration level of the majority of these sources, and the fact that their variability amplitudes were computed in the rest-frame 2–8 keV band, variable obscuration is not expected to play a significant role when their variability amplitudes are compared with our sources (see also Yang et al. 2016; Liu et al. 2017).

Figure 2 presents the variability amplitudes of the *Chandra* and *Swift* sources as a function of X-ray luminosity and shows for reference the CDF-S data grouped into seven luminosity bins, including ~15 sources per bin; our sources extend the X-ray luminosity range by an order of magnitude with respect to the CDF-S sample (see Figure 5 of Paper I; P17). The variability amplitudes of the *Chandra* sources in the left panel are based on their entire light curves, whereas only the *Chandra* epochs are considered when deriving these values in the right panel. In order to obtain a meaningful comparison with the CDF-S data, we extrapolated the X-ray luminosities of our sources to their rest-frame 2–8 keV band by assuming a photon index of $\Gamma = 2.0$ for each source in this band. Given this assumption and the redshifts involved, the fluxes of the

Chandra sources measured in the observed-frame 0.5–2 keV band, roughly correspond to those that would have been measured in their rest-frame 2–8 keV band; this conversion, therefore, is not expected to affect significantly the $\sigma_{\rm rms}^2$ values reported for the *Chandra* sources in Table 4.

As explained in Paper I, we prefer to compute the $\sigma_{\rm rms}^2$ values for our *Swift* sources using the observed-frame 0.2–10 keV band for their *Swift* observations. Filtering the *Swift* event files, in order to roughly match the rest-frame band of the *Chandra* sources, resulted in fluxes that are strongly correlated with the fluxes computed over the observed-frame 0.2–10 keV band. Furthermore, in spite of the factor of $\sim$2 drop in the number of counts as a result of this filtering, there is no significant change in the $\sigma_{\rm rms}^2$ values of the *Swift* sources; this is mainly due to the fact that their light curves display considerably larger variance with respect to the measurement errors (see Paper I). We conclude that the $\sigma_{\rm rms}^2$ values of the *Swift* sources (presented in Paper I) are also expected to remain roughly unchanged when converting to the rest-frame 2–8 keV band.

Figure 2 also shows mean luminosities and $\sigma_{\rm rms}^2$ values of the *Chandra* and *Swift* sources, separately, computed by averaging these properties from Paper I and Table 4; errors on these mean values were determined as their standard deviations divided by $\sqrt{4}$ and $\sqrt{3}$, respectively. The average luminosity of the *Swift* sources is larger than that of the *Chandra* sources by a factor of $\sim$2; this difference is smaller than the range of luminosities for sources in each of these groups.

Two main results emerge from Figure 2. First, at least for the highest luminosities probed in this work, there is no evidence that the X-ray variability amplitude increases with redshift, in spite of the extended temporal baseline of the *Chandra* sources, strengthening the findings of Paper I and P17. In fact, the new $\sigma_{\rm rms}^2$ values of the *Chandra* sources appear to be considerably *lower* with respect to their *Swift* counterparts. Second, the mean $\sigma_{\rm rms}^2$ value of the *Chandra* sources is broadly consistent with the general trend of decreasing variability amplitude as luminosity increases. These results are insensitive as to whether only the *Chandra* epochs or the entire light curves are considered for the *Chandra* sources.

The marked deviation of the *Swift* sources from the variability−luminosity trend cannot simply be explained by their small sample size or by the variety of systematics involved with respect to the CDF-S and *Chandra* sources (e.g., a mix of different observatories and sampling patterns). Potentially correcting for such systematics is not likely to reduce this deviation considerably; it is even less likely that the intrinsic $\sigma_{\rm rms}^2$ values of the *Swift* sources (i.e., if it were feasible to correct for such effects) lie well below those of their *Chandra* counterparts. As an extreme case, when considering only their *Swift* epochs, and thus the exposures with the lowest S/N (see Paper I), the two faintest *Swift* sources (PG 1247+267 and HS 1700+6416 that are also at the highest redshifts) exhibit $\sigma_{\rm rms}^2$ values that are both higher than, but roughly consistent within the errors with, those of the *Chandra* sources, when computed for the *Chandra* epochs for consistency and for comparing roughly similar rest-frame temporal baselines. For the brightest *Swift* source, PG 1634+706, this exercise yields no significant change in $\sigma_{\rm rms}^2$.

Although the rest-frame temporal baselines of the *Swift* sources are longer than those of the *Chandra* sources by a factor of $\approx$3, we show below that the variability levels of the former are consistently larger than those of the latter across almost all the timescales probed in this work (perhaps with an exception at the longest timescale). Additionally, it is likely that we have been probing our sources below their break frequencies, $\nu < \nu_{\rm b}$ (even for the first four epochs of the *Chandra* sources), assuming that these lie in the range $\nu_{\rm b} \approx 10^{-8} - 10^{-7}$ s^{-1}, corresponding to timescales of $\approx$1 yr (see Paper I for more details). Therefore, assuming a PSD slope of -1 at $\nu < \nu_{\rm b}$ (i.e., the longest timescales), the $\sigma_{\rm rms}^2$ values of the *Chandra* sources are expected to grow logarithmically as a function of time and gain only modest increases; thus, matching the temporal baselines of the *Chandra* sources to those of their *Swift* counterparts by simply extending the monitoring may not be sufficient for bringing their variability amplitudes to the levels currently exhibited by the latter group. The fact that the $\sigma_{\rm rms}^2$ values of the *Chandra* sources have not increased significantly with respect to Paper I is consistent with this assessment.

As we alluded to in Section 1, a combination of differences in basic physical properties, e.g., SMBH masses and accretion rates, between the *Swift* and *Chandra* sources, is also likely to contribute to the excess in X-ray variability of the former group with respect to the latter. Paper I presented estimates for the normalized accretion rates (in terms of the Eddington ratio, $L/L_{\rm Edd}$, where L is the bolometric luminosity) of two of our *Swift* sources, PG 1247+267 and PG 1634+706, having values of 0.5 and 0.3, respectively. While it is most likely that our *Chandra* sources have similar values (see, e.g., Trakhtenbrot et al. 2011), reliable estimates of the Eddington ratios for all our sources are required in order to relate any differences in X-ray variability to accretion rate effects in a statistically meaningful way.

In order to assess the effects of different accretion rates on the variability amplitudes of our sources, we consider a PSD model that assumes that both the break frequency, $\nu_{\rm b}$, and PSD normalization, A, depend on the Eddington ratio, $L/L_{\rm Edd}$, (i.e., Model 4 of P17). Specifically, this model takes the functional form of the PSD from Equation (5) and assumes that (1) $\nu_{\rm b} = (200 / 86400)\ L_{44}\ M_{\rm BH,6}^{-2}$ s^{-1}, where L_{44} and $M_{\rm BH,\,6}$ are the bolometric luminosity in units of 10^{44} erg s^{-1} and SMBH mass in units of $10^6\ M_\odot$, respectively (following the prescription of McHardy et al. 2006), and (2) PSD$(\nu_{\rm b}) = 3 \times 10^{-3}(L/L_{\rm Edd})^{-0.8}\ \nu_b^{-1}$ (as proposed by Ponti et al. 2012).

Figure 3, which is similar to Figure 2, shows the results stemming from this model with respect to our sources and those from the CDF-S sample of P17. One notable difference with respect to Figure 2 is that the CDF-S sources were regrouped into six bins representing four redshift intervals. This approach was taken in order to minimize the effect of decreasing rest-frame temporal baseline[15] as a function of redshift, given the uniform, observed-frame temporal baseline of $\sim$17 years for the 7 Ms exposure of the CDF-S (see, e.g., Papadakis et al. 2008, P17). All six X-ray epochs are considered for our *Chandra* sources. Each model (solid lines in Figure 3) takes into account the rest-frame temporal baseline associated with the mean redshift in each redshift interval, while allowing the best-fit Eddington ratio to vary between each redshift interval with $L/L_{\rm Edd}$ values ranging between 0.04 and 0.09; see Table 1 of P17. Four additional similar models with $L/L_{\rm Edd} = 0.06$ and $L/L_{\rm Edd} = 0.50$ (thin and thick solid

---

[15] The rest-frame temporal baseline determines the $\nu_{\rm min}$ limit in Equation (4), required for computing the variance.
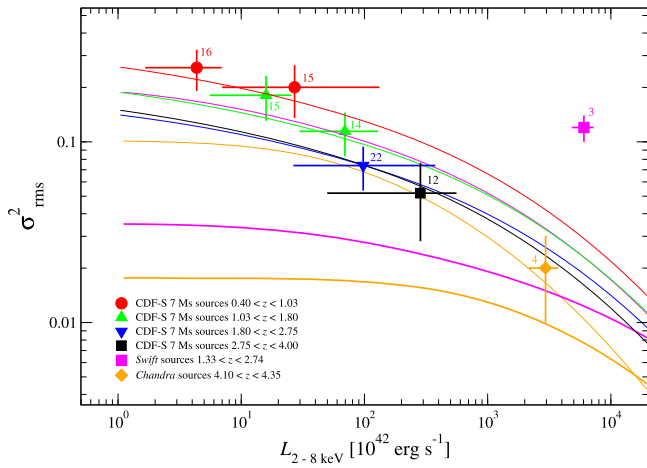
Figure 3. Similar to the left panel of Figure 2, except that the CDF-S sources are binned into four redshift intervals. Circles, upward triangles, downward triangle, and filled square represent average luminosities and $\sigma^2_{\rm rms}$ values of X-ray-selected AGNs from the 7 Ms exposure of the CDF-S survey at $0.40 < z < 1.03$, $1.03 < z < 1.80$, $1.80 < z < 2.75$, and $2.75 < z < 4.00$, respectively (adapted from P17). The magenta square and orange diamond represent the average luminosities and $\sigma^2_{\rm rms}$ values of our *Swift* and *Chandra* sources, respectively (with six epochs, per source, considered for the latter). The number of sources is indicated next to each bin. Red, green, blue, and black thin solid lines represent the most acceptable $\sigma^2_{\rm rms}$ vs. $L_{2-8\,\rm keV}$ models, having $L/L_{\rm Edd} = 0.04, 0.06, 0.09$, and 0.08, corresponding to the bins with matching color, in order of increasing redshift. The magenta and orange thin (thick) solid lines represent similar models corresponding to the *Swift* and *Chandra* bins, respectively, but having $L/L_{\rm Edd} = 0.06$ ($L/L_{\rm Edd} = 0.50$). The models with higher Eddington ratios predict smaller variability amplitudes at a given luminosity.

lines, respectively) are included in Figure 3 for our *Swift* and *Chandra* sources (in magenta and orange, respectively). The first pair of these models (thin lines) corresponds to the mean Eddington ratio, $\langle L/L_{\rm Edd}\rangle \simeq 0.06$, obtained from Model 4 of P17 for all the CDF-S sources; these models predict significantly larger variability amplitudes with respect to the second pair (thick lines). In this scenario, the variability amplitudes of the *Swift* sources, which are inconsistent with any of these models, may imply extremely low accretion rates. Clearly, this implication cannot be reconciled with the extremely high values derived from archival optical and X-ray spectroscopy, as well as from the extremely high luminosities, of these sources (see, e.g., Shemmer et al. 2008, Paper I).

Figure 3 appears to portray a mixed picture about X-ray variability amplitudes of AGNs. While the *Chandra* sources seem to follow the general trend of a decreasing amplitude as a function of luminosity, and Eddington ratios consistent with $L/L_{\rm Edd} \lesssim 0.50$, as can be expected for such sources, the *Swift* sources stand out by exhibiting excess variability given their luminosities as well as unrealistically implied small Eddington ratios according to our variability models. In order to reconcile this discrepancy, additional, large-scale X-ray monitoring is required across the widest ranges in the luminosity−redshift parameter space, particularly for highly luminous RQQs, including our sources, in order to improve the currently limited statistics. Nevertheless, following the interpretation of Figure 2, one clear result that stems from this analysis is the fact that the X-ray variability amplitude does not increase toward higher redshifts, as opposed to what has been suspected in earlier studies (see Section 1). The only apparent trend involving
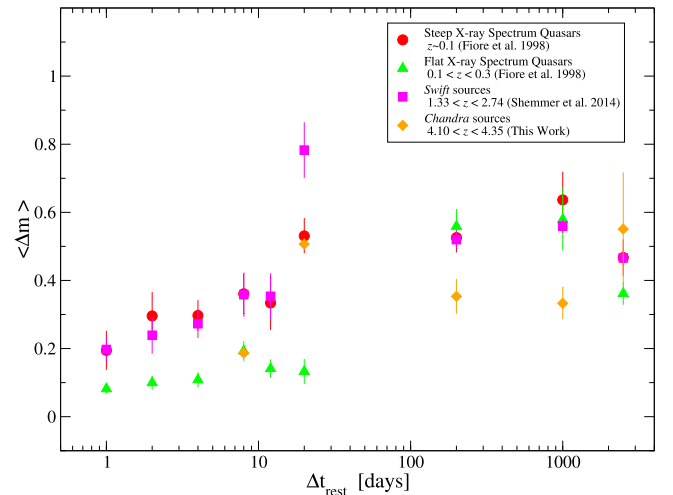

Figure 4. Ensemble SF of the *Chandra* sources (diamonds) compared to the ensemble SF of the *Swift* sources from Paper I (squares) as well as the ensemble SFs of the steep and flat X-ray-spectrum quasars at low redshift, marked by circles and triangles, respectively, adapted from Fiore et al. (1998). Average magnitude difference in each time bin is plotted as a function of rest-frame time interval. Except for the longest timescale, the ensemble SF of sources at $z \simeq 4.2$ is significantly lower than that of similarly luminous RQQs at intermediate redshifts.

redshift in this context, which excludes the three *Swift* sources, is that associated with the luminosity−redshift degeneracy inherent in flux-limited samples.

3.3. Variability Timescales

In order to disentangle the variability dependence on timescale from that on luminosity, which prevents a simpler interpretation of Figure 2, a variability SF can be informative. This is a useful means of analyzing a sparsely sampled light curve composed of a small number of epochs, which would otherwise produce a low-quality PSD function unsuitable for meaningful analysis (e.g., Emmanoulopoulos et al. 2010; Vagnetti et al. 2011, 2016; Middei et al. 2017). The SFs of our *Swift* sources were computed in Paper I. However, with only six X-ray epochs per source, sampled in a non-systematic fashion, even a SF is not sufficiently sensitive for performing a meaningful temporal analysis of each individual *Chandra* source. Nevertheless, these data do allow us to construct an ensemble SF, providing the first qualitative assessment of the variability patterns and timescales of RQQs at $z \simeq 4.2$. We computed this ensemble SF following the steps outlined in Paper I, by averaging SF values (i.e., Δm) of all the *Chandra* sources in each rest-frame time bin, using the SF definition from Fiore et al. (1998),

$$\Delta m_{ji} = |2.5 \log\left[f(t_j)/f(t_i)\right]|, \qquad (6)$$

where $f(t_j)$ and $f(t_i)$ are the fluxes of each source at epochs t_j and t_i, respectively, such that $t_j > t_i$, and every t_i is measured in rest-frame days since the first epoch (i.e., $t_1 = 0$); time bins were taken with limits at 1, 2, 4, 8, 12, 20, 200, 1000, and 2500 days, matching those of Fiore et al. (1998) and Paper I.

The ensemble SF of our *Chandra* sources, composed of five timescale bins, is plotted in Figure 4 against the ensemble SFs of our *Swift* sources (Paper I) and those of nearby, steep and flat X-ray-spectrum quasars from Fiore et al. (1998). Figure 4

shows that, except for the longest timescale, corresponding to about five years in the rest frame, the X-ray variability of sources at $z \simeq 4.2$ is significantly lower than that of similarly luminous sources at lower redshifts (i.e., the *Swift* sources) in the other four timescales probed, ranging from about a week to three years in the rest frame. This result is consistent with the main finding of Section 3.2. A similar trend is observed with respect to the steep X-ray spectrum sources, except for the bin at 20 days in the rest frame where the X-ray variability of the latter is consistent with that of the *Chandra* sources. A more complicated behavior is observed with respect to the flat X-ray spectrum sources. The latter vary significantly more than our *Chandra* sources in the 200- and 1000-day bins, as opposed to the 20-day bin, whereas their X-ray variability is consistent with that of the *Chandra* sources in the 8-day bin. This more complex SF behavior may be a manifestation of two competing effects where, at least at the shortest timescale probed, the suppressed variability of the *Chandra* sources (given their high luminosities) is comparable to the effect of low accretion rates in the flat-X-ray spectrum (low-luminosity) sources.

When only their *Chandra* epochs are considered, the ensemble SF of the *Chandra* sources does not differ significantly from that displayed in Figure 4, except for a lack of the longest-timescale bin, corresponding to the time difference between the *Chandra* and *ROSAT* observations of Q 0000−263 and BR 0351−1034. This last data point, an average of two Δm values at $\Delta t \sim 1600$ days in the rest frame, is consistent, within the errors, with the corresponding bins of the three other quasar groups, and also with all the other SF bins of the *Chandra* sources, except for the shortest-timescale bin. Additional *Chandra* monitoring, extending over at least another decade in the observed frame, is required to minimize cross-calibration effects among the different observatories and to better characterize the ensemble SF of the *Chandra* sources on all rest-frame timescales probed in this work.

The fact that the ensemble SF of the *Chandra* sources is rather flat and does not increase significantly at rest-frame timescales of $\approx 20-1000$ days may naturally explain why the variability amplitudes of these sources remained constant, within the errors, in spite of the extended temporal baseline and the 50% increase in the number of X-ray epochs with respect to Paper I (see Section 3.1). It should be noted, though, that the temporal baselines of the *Chandra* sources have been extended by only $\sim$130–210 days in the rest frame, corresponding to fractional increases of $\sim$10%–20% in the temporal baseline. As noted in Sections 3.1 and 3.2, such modest increases, coupled with the expected power-law slope of -1 for a typical PSD function at $\nu < \nu_b$, should result, at most, in a logarithmic increase in σ_{rms}^2, which may be detectable over considerably longer timescales than those probed here. In principle, an extended monitoring campaign, yielding an improved SF, is required for tracing the PSD functions of these sources and placing meaningful constraints on their power-law slopes.

3.4. Ground-Based Photometry

Our *Chandra* Cycles 14 and 15 observations were complemented by near-simultaneous ground-based photometry in order to search for connections between X-ray and rest-frame UV variations. These observations were performed at the Tel Aviv University Wise Observatory (WO), using the 1 m and C18 18″ telescopes, and at Las Campanas Observatory (LCO), using the du Pont 2.5 m telescope. Images of BR 0351−1034,

PSS 0926+3055, and PSS 1326+0743 were obtained with the WO 1 m telescope using the PI CCD camera, which has a $13' \times 13'$ field of view with a scale of 0″58 pix^{-1}, using the Sloan Digital Sky Survey g', r', i', and z' filters (Fukugita et al. 1996) and Bessell B, V, R, and I filters, depending on their availability each night. Observations of Q 0000−263 were performed with the WO C18 telescope using the SBIG STL-6303E CCD, which has a $75' \times 50'$ field of view with a scale of 1″47 pix^{-1}, using Bessell B, V, and R filters. Additional observations of BR 0351−1034 were obtained at LCO in the Johnson V and R bands with the Wide Field CCD camera, which has a scale of 0″484 pix^{-1} and is equipped with a WF4K detector.[16]

We followed the reduction and analysis procedures of Paper I to obtain final, calibrated magnitudes and rest-frame UV flux densities of the *Chandra* sources, which are reported in Tables 5 and 6. Briefly, these include image reduction using standard IRAF[17] routines, light-curve calibration (e.g., Netzer et al. 1996), and flux calibration based on the magnitudes of nearby field stars, using prescriptions described in detail in Section 3.3.2 of Paper I. The flux calibrations may be systematically uncertain by up to 0.5 mag due to these calibration prescriptions, but these systematics are not accounted for in the uncertainties quoted in Tables 5 and 6; the uncertainties include only fluctuations due to photon statistics and scatter from measurements of the non-variable field stars.

The light-curve calibration procedure depends on the entire image set obtained for each source, starting from the beginning of our monitoring campaign. Hence, source magnitudes, and therefore flux densities, can change in earlier epochs. Inspection of Tables 5 and 6, which provide the photometric data for the entire campaign, shows that in the vast majority of cases the difference in magnitude with respect to Paper I is negligible. The only exceptions are the r' and i' magnitudes of PSS 0926+3055 in 2012 February 4, which have decreased by $\sim$0.1 mag, but are consistent at the $\sim 2\sigma$ level with the corresponding values reported in Paper I.

Table 6 provides flux densities at rest-frame 1450 Å for each ground-based epoch and the band from which these were determined. The band choice is based on maximizing the photometric S/N, minimizing the difference between the band effective wavelength and 1450$(1+z)$ Å, and minimizing emission-line contamination. The flux densities at rest-frame 1450 Å, and their errors, were extrapolated from the flux densities at the effective wavelengths of the respective bands, assuming a continuum of the form $f_\nu \propto \nu^{-0.5}$ (Vanden Berk et al. 2001) in the relevant wavelength range, and using the magnitude-to-flux-density conversion factors from Bessell et al. (1998) and Fukugita et al. (1996). Flux densities at rest-frame 2500 Å and their errors (not shown) were obtained in the same manner. Together with the flux densities at rest-frame 2 keV (Table 2) and their errors (derived from errors on the X-ray fluxes in Table 3), these values were used for computing the optical-to-X-ray spectral slope, α_{ox}, and its error, where α_{ox} is defined as $\log(f_{2\,keV}/f_{2500\,Å})/\log(\nu_{2\,keV}/\nu_{2500\,Å})$, and $f_{2\,keV}$ ($f_{2500\,Å}$) is the flux density at rest-frame 2 keV (2500 Å).

Table 6 lists the shortest time separations between the *Chandra* observations and the ground-based photometry; these

---

[16] http://www.lco.cl/draft/direct-ccd-users-manual
[17] IRAF (Image Reduction and Analysis Facility) is distributed by the National Optical Astronomy Observatories, which are operated by AURA, Inc, under cooperative agreement with the National Science Foundation.

Table 5
Ground-based Photometry

Quasar	Obs.	Obs. Date	g' (mag)	r' (mag)	i' (mag)	z' (mag)	B (mag)	V (mag)	R (mag)	I (mag)
Q 0000−263	WO1m	2011 Sep 4	18.93 ± 0.02	17.45 ± 0.02	⋯	⋯	19.58 ± 0.04	18.23 ± 0.02	17.16 ± 0.02	⋯
	WO1m	2012 Sep 14	18.93 ± 0.03	17.48 ± 0.01	⋯	⋯	19.45 ± 0.09	18.28 ± 0.02	17.18 ± 0.03	⋯
	WO1m	2012 Sep 15	18.97 ± 0.02	17.48 ± 0.01	⋯	⋯	19.53 ± 0.04	18.26 ± 0.02	17.17 ± 0.01	⋯
	WOC18	2013 Sep 5	⋯	⋯	⋯	⋯	19.62 ± 0.10	18.37 ± 0.04	17.21 ± 0.02	⋯
	WOC18	2014 Sep 19	⋯	⋯	⋯	⋯	⋯	18.18 ± 0.04	17.07 ± 0.03	⋯
	WOC18	2014 Sep 20	⋯	⋯	⋯	⋯	19.40 ± 0.06	18.14 ± 0.04	17.09 ± 0.02	⋯
BR 0351−1034	WO1m	2011 Mar 3	⋯	19.39 ± 0.06	⋯	⋯	⋯	⋯	19.24 ± 0.05	⋯
	WO1m	2011 Mar 5	⋯	19.33 ± 0.04	⋯	⋯	⋯	⋯	⋯	⋯
	WO1m	2011 Sep 26	⋯	19.33 ± 0.03	⋯	⋯	⋯	20.59 ± 0.09	19.29 ± 0.04	⋯
	LCO	2011 Oct 29	⋯	⋯	⋯	⋯	22.79 ± 0.11	20.55 ± 0.02	19.35 ± 0.03	⋯
	WO1m	2013 Aug 18	⋯	⋯	⋯	⋯	⋯	20.39 ± 0.09	19.23 ± 0.08	⋯
	WO1m	2014 Nov 25	⋯	⋯	⋯	⋯	⋯	20.54 ± 0.11	19.14 ± 0.06	⋯
	LCO	2014 Nov 26	⋯	⋯	⋯	⋯	⋯	20.41 ± 0.04	19.10 ± 0.04	⋯
PSS 0926+3055	WO1m	2011 Mar 4	18.45 ± 0.01	17.13 ± 0.01	17.01 ± 0.01	17.22 ± 0.03	⋯	17.83 ± 0.02	16.90 ± 0.01	16.60 ± 0.02
	WO1m	2012 Feb 4	18.55 ± 0.05	17.23 ± 0.04[a]	17.05 ± 0.05[a]	⋯	⋯	17.94 ± 0.05	17.11 ± 0.08	16.66 ± 0.04
	WO1m	2013 May 15	⋯	⋯	⋯	⋯	19.20 ± 0.07	17.91 ± 0.01	16.92 ± 0.01	16.58 ± 0.01
	WO1m	2014 Jan 23	18.43 ± 0.03	17.13 ± 0.02	17.00 ± 0.02	⋯	⋯	17.91 ± 0.03	16.91 ± 0.02	16.41 ± 0.02
PSS 1326+0743	WO1m	2011 Mar 8	19.15 ± 0.10	⋯	⋯	⋯	⋯	18.47 ± 0.03	17.48 ± 0.02	16.88 ± 0.03
	WO1m	2011 Mar 14	19.28 ± 0.03	17.82 ± 0.10	17.51 ± 0.10	17.15 ± 0.03	⋯	18.47 ± 0.02	17.49 ± 0.02	16.77 ± 0.12
	WO1m	2012 May 1	⋯	17.79 ± 0.06	17.61 ± 0.07	⋯	⋯	18.52 ± 0.14	17.59 ± 0.07	16.69 ± 0.09
	WO1m	2013 Dec 15	19.46 ± 0.12	17.81 ± 0.03	17.61 ± 0.09	⋯	⋯	18.64 ± 0.10	17.54 ± 0.04	16.96 ± 0.10
	WO1m	2013 Dec 16	19.25 ± 0.06	17.80 ± 0.02	17.60 ± 0.04	⋯	20.07 ± 0.20	18.66 ± 0.06	17.53 ± 0.02	16.90 ± 0.03

Note.
[a] Magnitude change with respect to Paper I (see the text for more details).

Table 6
Rest-frame UV Flux Densities and α_{ox} Data for the *Chandra* Sources

Quasar	JD	F_{λ}[a]	Obs.	Band	α_{ox}[b]	Δt[c]
Q 0000−263	2455809.5	2.41 ± 0.04	WO1m	R	−1.74 ± 0.02	1.4
	2456185.5	2.35 ± 0.07	WO1m	R	−1.76 ± 0.03	2.4
	2456186.5	2.39 ± 0.03	WO1m	R	⋯	⋯
	2456541.5	2.29 ± 0.05	WOC18	R	−1.82 ± 0.03	0.2
	2456920.5	2.62 ± 0.08	WOC18	R	−1.76 ± 0.03	0.7
	2456921.5	2.57 ± 0.05	WOC18	R	⋯	⋯
BR 0351−1034	2455624.2	0.33 ± 0.02	WO1m	R	⋯	⋯
	2455626.2	0.37 ± 0.01	WO1m	r'	⋯	⋯
	2455831.5	0.31 ± 0.01	WO1m	R	$-1.65^{+0.05}_{-0.06}$	0.7
	2455864.8	0.30 ± 0.01	LCO	R	−1.67 ± 0.06	0.4
	2456523.5	0.33 ± 0.03	WO1m	R	−1.57 ± 0.04	6.0
	2456987.5	0.36 ± 0.02	WO1m	R	⋯	⋯
	2456988.5	0.37 ± 0.01	LCO	R	−1.62 ± 0.05	0.2
PSS 0926+3055	2455625.2	2.81 ± 0.06	WO1m	I	−1.73 ± 0.03	0.3
	2455962.3	2.68 ± 0.11	WO1m	I	−1.78 ± 0.04	4.4
	2456428.5	2.87 ± 0.03	WO1m	I	−1.69 ± 0.03	0.8
	2456681.5	3.36 ± 0.07	WO1m	I	−1.73 ± 0.03	1.2
PSS 1326+0743	2455629.6	1.76 ± 0.04	WO1m	R	−1.65 ± 0.03	0.4
	2455635.5	1.74 ± 0.03	WO1m	R	⋯	⋯
	2456049.3	1.59 ± 0.11	WO1m	R	−1.64 ± 0.03	0.3
	2456642.5	1.65 ± 0.06	WO1m	R	−1.67 ± 0.04	1.9
	2456643.5	1.67 ± 0.04	WO1m	R	⋯	⋯

Notes. For each source, α_{ox} is given only for the shortest time separations between the optical and *Chandra* observations.
[a] Flux density at rest-frame 1450 Å in units of 10^{-16} erg cm^{-2} s^{-1} Å^{-1}, extrapolated from the flux density at the effective wavelength of the respective band, assuming a continuum of the form $f_{\nu} \propto \nu^{-0.5}$ (Vanden Berk et al. 2001).
[b] Errors at the 1σ level on α_{ox} were derived according to Section 1.7.3 of Lyons (1991), given the errors on the rest-frame UV flux densities and the errors on the X-ray fluxes from Table 3.
[c] Rest-frame days between the ground-based and *Chandra* observations.

are on the order of ≈1 day in the rest frame. Based on the photometry in Table 5, we do not consider these time delays to be significant as we do not detect large rest-frame UV flux variations on such relatively short timescales. However, we do detect such variations at a level of up to ∼25% on considerably longer timescales, ≈100 days in the rest frame, consistent with observations of luminous, high-redshift quasars monitored on similar timescales (e.g., Kaspi et al. 2007). Half of our sources, Q 0000−263 and PSS 0926+3055, exhibit changes in α_{ox} at a level of $\Delta\alpha_{ox} = 0.08$ and $\Delta\alpha_{ox} = 0.09$ between Cycles 12 and 14 and between Cycles 13 and 14, respectively (Table 6), reflecting primarily the factor of ∼2 difference between the *Chandra* fluxes of the sources in each of these pairs of Cycles (Tables 3 and 5); the α_{ox} values of the other half are consistent, within the errors, across all epochs. The significant α_{ox} variations of Q 0000−263 and PSS 0926+3055 are consistent with recent findings suggesting that X-ray variability is a major contributor to the scatter in α_{ox}, when the optical-UV and X-ray observations are not contemporaneous (see, e.g., Paper I and references therein).

4. Summary

Traditional X-ray time-domain surveys are unable to provide the necessary long-term variability information on the most luminous and distant quasars known. Deep surveys, such as the CDF-S, are limited by area and thus cannot probe the luminous tail of the AGN luminosity function. Wider-area surveys, on the other hand, typically lack the extended temporal baseline, and are limited by depth, thus limiting the redshift coverage.

Our strategy of targeted X-ray monitoring of luminous RQQs at high redshift is, therefore, a necessary complementary approach.

In this work, we present extended *Chandra* monitoring of four luminous RQQs at $4.10 \leqslant z \leqslant 4.35$ (i.e., the *Chandra* sources), each having a total of six X-ray epochs, enabling a qualitative assessment of the X-ray variability properties of such sources. For half of these sources, four of the epochs originate from *Chandra* observations, and the rest-frame temporal baseline spans ∼1600 days; for the other half, there are five *Chandra* epochs and a rest-frame temporal baseline spanning ∼850 days. During the most recent ∼220 days in the rest frame of each source, i.e., during the most recent four *Chandra* epochs, we also obtained near-simultaneous ground-based photometry, covering the sources' rest-frame UV band. Our main findings are as follows.

1. When compared with X-ray variability of AGNs across wide ranges of luminosity and redshift, our *Chandra* sources appear to follow the well-known trend of decreasing X-ray variability amplitude with increasing X-ray luminosity, and there is no evidence for increased X-ray variability with increasing redshift. This result strengthens the tentative findings of Paper I as well as those of P17 and does not support certain evolutionary scenarios for AGN X-ray variability that were proposed in earlier studies.

2. In spite of the 50% increase in the number of X-ray epochs and the extension of the temporal baseline by ∼130–210 days in the rest frame, the X-ray variability

amplitudes of our *Chandra* sources have not changed significantly with respect to our initial measurements (Paper I).

3. Three comparably luminous RQQs at $1.33 \leqslant z \leqslant 2.74$ (i.e., the *Swift* sources) display excess X-ray variability and deviate considerably from the variability−luminosity trend. It is yet unclear whether this deviation is related to a basic physical property, such as the accretion rate, or due to large uncertainties stemming from the known biases involved with the limited variability data and the sparse sampling of the light curves.

4. An ensemble X-ray variability SF for RQQs at $\langle z \rangle \simeq 4.2$ is relatively flat and does not show evidence of increasing variability at rest-frame timescales ranging from ≈ 20 to ≈ 1000 days. This SF is also generally lower than the ensemble SF of the *Swift* sources, consistent with our measurements of X-ray variability amplitudes.

5. Our *Chandra* sources display rest-frame UV flux variations at a level of up to $\sim 25\%$ on timescales not shorter than ≈ 100 days in the rest frame, consistent with similar behavior observed for luminous, high-redshift quasars.

6. Half of our *Chandra* sources, Q 0000−263 and PSS 0926+3055, display significant α_{ox} variations at a level of up to $\Delta \alpha_{\mathrm{ox}} = 0.09$, dominated by X-ray variability; this supports recent claims that X-ray variability contributes significantly to the scatter in α_{ox} measurements originating from non-contemporaneous optical-UV and X-ray data.

We plan to continue the monitoring of our *Chandra* sources, in order to (1) obtain meaningful temporal statistics that would allow us to improve and better characterize our variability measures, such as the amplitudes and temporal behavior, (2) extend the temporal baseline and trace the $\nu \ll \nu_{\mathrm{b}}$ PSD regime, and (3) enable a meaningful comparison with respect to X-ray variability of larger samples of sources at similar or higher redshifts that will be monitored with upcoming X-ray missions such as *Athena*. The *Chandra* monitoring will be particularly important and complementary to the *eROSITA* survey, which may detect sources at $z > 4$, but may not provide light curves with adequate S/N for such sources.

ORCID iDs

Ohad Shemmer https://orcid.org/0000-0003-4327-1460
W. N. Brandt https://orcid.org/0000-0002-0167-2453
Maurizio Paolillo https://orcid.org/0000-0003-4210-7693
Cristian Vignali https://orcid.org/0000-0002-8853-9611

References

Allevato, V., Paolillo, M., Papadakis, I., & Pinto, C. 2013, ApJ, 771, 9
Almaini, O., Lawrence, A., Shanks, T., et al. 2000, MNRAS, 315, 325
Bessell, M. S., Castelli, F., & Plez, B. 1998, A&A, 333, 231
Bonzini, M., Padovani, P., Mainieri, V., et al. 2013, MNRAS, 436, 3759
Dickey, J. M., & Lockman, F. J. 1990, ARA&A, 28, 215
Eadie, W. T., Drijard, D., & James, F. E. 1971, Statistical Methods in Experimental Physics (Amsterdam: North-Holland)
Emmanoulopoulos, D., McHardy, I. M., & Uttley, P. 2010, MNRAS, 404, 931
Ferrero, E., & Brinkmann, W. 2003, A&A, 402, 465
Fiore, F., Laor, A., Elvis, M., Nicastro, F., & Giallongo, E. 1998, ApJ, 503, 607
Freeman, P. E., Kashyap, V., Rosner, R., & Lamb, D. Q. 2002, ApJS, 138, 185
Fukugita, M., Ichikawa, T., Gunn, J. E., et al. 1996, AJ, 111, 1748
Garmire, G. P., Bautz, M. W., Ford, P. G., Nousek, J. A., & Ricker, G. R. 2003, Proc. SPIE, 4851, 28
Gehrels, N. 1986, ApJ, 303, 336
Gehrels, N., Chincarini, G., Giommi, P., et al. 2004, ApJ, 611, 1005
González-Martín, O., & Vaughan, S. 2012, A&A, 544, A80
Grupe, D., Mathur, S., Wilkes, B., & Elvis, M. 2004, AJ, 127, 1
Grupe, D., Mathur, S., Wilkes, B., & Osmer, P. 2006, AJ, 131, 55
Kaspi, S., Brandt, W. N., Maoz, D., et al. 2007, ApJ, 659, 997
Kaspi, S., Brandt, W. N., & Schneider, D. P. 2000, AJ, 119, 2031
Kellermann, K. I., Sramek, R., Schmidt, M., Shaffer, D. B., & Green, R. 1989, AJ, 98, 1195
Kraft, R. P., Burrows, D. N., & Nousek, J. A. 1991, ApJ, 374, 344
La Franca, F., Bianchi, S., Ponti, G., Branchini, E., & Matt, G. 2014, ApJL, 787, L12
Lanzuisi, G., Ponti, G., Salvato, M., et al. 2014, ApJ, 781, 105
Lawrence, A., & Papadakis, I. 1993, ApJL, 414, L85
Liu, T., Tozzi, P., Wang, J.-X., et al. 2017, ApJS, 232, 8
Luo, B., Brandt, W. N., Xue, Y. Q., et al. 2017, ApJS, 228, 2
Lyons, L. (ed.) 1991, A Practical Guide to Data Analysis for Physical Science Students (Cambridge: Cambridge Univ. Press)
Manners, J., Almaini, O., & Lawrence, A. 2002, MNRAS, 330, 390
Markowitz, A., Edelson, R., Vaughan, S., et al. 2003, ApJ, 593, 96
McHardy, I. M., Koerding, E., Knigge, C., Uttley, P., & Fender, R. P. 2006, Natur, 444, 730
Middei, R., Vagnetti, F., Bianchi, S., et al. 2017, A&A, 599, A82
Nandra, K., George, I. M., Mushotzky, R. F., Turner, T. J., & Yaqoob, T. 1997, ApJ, 476, 70
Netzer, H., Heller, A., Loinger, F., et al. 1996, MNRAS, 279, 429
O'Neill, P. M., Nandra, K., Papadakis, I. E., & Turner, T. J. 2005, MNRAS, 358, 1405
Paolillo, M., Papadakis, I., Brandt, W. N., et al. 2017, MNRAS, 471, 4398 (P17)
Paolillo, M., Schreier, E. J., Giacconi, R., Koekemoer, A. M., & Grogin, N. A. 2004, ApJ, 611, 93
Papadakis, I. E., Chatzopoulos, E., Athanasiadis, D., Markowitz, A., & Georgantopoulos, I. 2008, A&A, 487, 475
Ponti, G., Papadakis, I., Bianchi, S., et al. 2012, A&A, 542, A83
Shemmer, O., Brandt, W. N., Netzer, H., Maiolino, R., & Kaspi, S. 2008, ApJ, 682, 81
Shemmer, O., Brandt, W. N., Paolillo, M., et al. 2014, ApJ, 783, 116 (Paper I)
Shemmer, O., Brandt, W. N., Vignali, C., et al. 2005, ApJ, 630, 729
Spergel, D. N., Bean, R., Doré, O., et al. 2007, ApJS, 170, 377
Townsley, L. K., Broos, P. S., Garmire, G. P., & Nousek, J. A. 2000, ApJL, 534, L139
Trakhtenbrot, B., Netzer, H., Lira, P., & Shemmer, O. 2011, ApJ, 730, 7
Turner, T. J., George, I. M., Nandra, K., & Turcan, D. 1999, ApJ, 524, 667
Uttley, P., McHardy, I. M., & Papadakis, I. E. 2002, MNRAS, 332, 231

Vagnetti, F., Middei, R., Antonucci, M., Paolillo, M., & Serafinelli, R. 2016, A&A, 593, A55

Vagnetti, F., Turriziani, S., & Trevese, D. 2011, A&A, 536, A84

Vanden Berk, D. E., Richards, G.T., Bauer, A., et al. 2001, AJ, 122, 549

Vaughan, S., Edelson, R., Warwick, R. S., & Uttley, P. 2003, MNRAS, 345, 1271

Vignali, C., Brandt, W. N., Fan, X., et al. 2001, AJ, 122, 2143

Vignali, C., Brandt, W. N., Schneider, D. P., Garmire, G. P., & Kaspi, S. 2003, AJ, 125, 418

Weisskopf, M. C., Tananbaum, H. D., Van Speybroeck, L. P., & O'Dell, S. L. 2000, Proc. SPIE, 4012, 2

Yang, G., Brandt, W. N., Luo, B., et al. 2016, ApJ, 831, 145